

Origami Tomography

by

Jason Ku

B.S., Massachusetts Institute of Technology (2009)

Submitted to the Department of Mechanical Engineering
in partial fulfillment of the requirements for the degree of

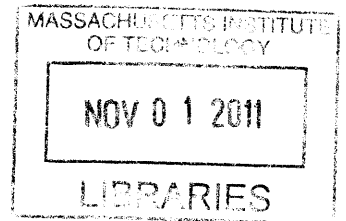
Master of Science in Mechanical Engineering

at the

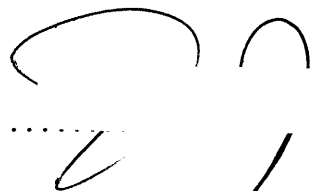
MASSACHUSETTS INSTITUTE OF TECHNOLOGY

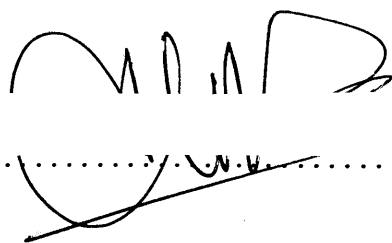
September 2011

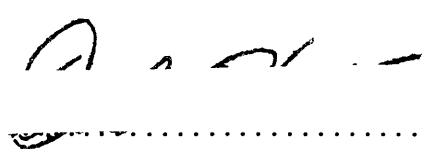
ARCHIVES



© Massachusetts Institute of Technology 2011. All rights reserved.

Author 
Department of Mechanical Engineering
August 5, 2011

Certified by 
George Barbastathis
Professor
Thesis Supervisor

Accepted by 
David E. Hardt
Chairman, Department Committee on Graduate Theses

Origami Tomography

by

Jason Ku

Submitted to the Department of Mechanical Engineering
on August 5, 2011, in partial fulfillment of the
requirements for the degree of
Master of Science in Mechanical Engineering

Abstract

This thesis analyzes two dimensional tomographic imaging of surface objects with negligible volume, concentrating on piecewise linear surfaces similar to folded origami. In contrast to the large number of projections usually necessary in traditional tomographic imaging, information is extracted directly from a small number of Radon projections. Furthermore, piecewise linear chains are shown to be fully characterized from just two sampled Radon projections, assuming perfect sampling resolution of these projections.

Thesis Supervisor: George Barbastathis
Title: Professor

Acknowledgments

I want to dedicate this thesis to my family: my father, David, my mother, Karen, my brother, Ben, and my twin sister, Sarah all of whom I am extremely fortunate to have as the solid foundation of my life. Thank you for supporting me no matter what road I choose to travel.

I must extend my deepest thanks to my advisor for being thoroughly supportive and understanding in my many ups and downs. Additional thanks to everyone in the 3D Optical Systems group for making my time as a Masters student thoroughly enjoyable, especially to Se Baek Oh, Nick Loomis, Laura Waller, Lei Tian, and Justin Lee for keeping me sane.

Contents

| | | |
|----------|---|-----------|
| 1 | Introduction | 13 |
| 2 | Tomography | 17 |
| 2.1 | Radon Transform | 17 |
| 2.2 | Fourier Slice Theorem | 18 |
| 2.3 | Filtered Backprojection | 19 |
| 2.4 | X-ray transform | 20 |
| 2.5 | Beer-Lambert Law | 21 |
| 2.6 | Two Dimensional Radon Transforms | 21 |
| 2.7 | Compressive Sensing | 23 |
| 3 | Surface Attenuation Model | 25 |
| 3.1 | Hypersurfaces | 25 |
| 3.2 | Attenuation Function of Hyperplanes | 26 |
| 3.3 | Attenuation Function of Hypersurfaces | 28 |
| 4 | Identification of Surface Objects | 29 |
| 4.1 | Identification of a Point Object | 29 |
| 4.2 | Identification of a Line Segment Object | 33 |
| 4.2.1 | Two Projections | 36 |
| 4.2.2 | Three Projections | 38 |
| 4.3 | Identification of Two Connected Line Segments | 39 |
| 4.3.1 | Random Projections | 41 |

| | | |
|----------|---|-----------|
| 4.3.2 | Two Projections | 42 |
| 4.4 | Identification of Piecewise Linear Graphs | 45 |
| 4.5 | Identification of Curved Surface Objects | 45 |
| 5 | Conclusion | 47 |
| A | Notation | 49 |
| B | MATLAB Code | 51 |
| B.1 | Obtaining Projection Data | 51 |
| B.2 | Detecting Object Vertices | 53 |
| B.3 | Detecting Object Edges | 56 |
| B.4 | Plotting | 60 |

List of Figures

| | | |
|-----|---|----|
| 2-1 | Geometry of the Radon transform. | 18 |
| 3-1 | Geometry of a line projection $\langle \mathbf{x}, \boldsymbol{\theta} \rangle = s$ crossing a hyperplane \mathbf{P}^{n-1} of thickness $2r$ in \mathbb{R}^2 at angle ϕ given by $\sqrt{1 - \langle \boldsymbol{\theta}, \boldsymbol{\eta} \rangle^2} = \sin \phi$ | 26 |
| 4-1 | Nonzero locations of the Radon transform sinogram of a point in \mathbb{R}^2 | 31 |
| 4-2 | Nonzero locations of the Radon transform circlegram of a point in \mathbb{R}^2 | 32 |
| 4-3 | Intensity converted Radon transform sinogram of generic line segment L with $\alpha = 0.2$ | 35 |
| 4-4 | Intensity converted Radon transform circlegram of generic line segment L with $\alpha = 0.2$. A “+” marks the origin, with L drawn in black. | 36 |
| 4-5 | Radon transform circlegram for ten evenly spaced points of generic line segment L | 36 |
| 4-6 | Backprojections and two possible circlegrams for one pair of projections of a unknown line segment object, either L or L' | 37 |
| 4-7 | Intensity converted Radon transform sinogram of generic line segment L with $\alpha = 0.2$ | 40 |
| 4-8 | Intensity converted Radon transform circlegram of generic line segment L with $\alpha = 0.2$. A “+” marks the origin, with L drawn in black. | 41 |
| 4-9 | Backprojections for two generic Radon projections of a unknown connected line segment object L_2 . Possible vertex positions are circled and numbered. | 43 |

List of Tables

| | | |
|-----|---|----|
| 4.1 | Vertex ordering of the 18 possible two segment paths given two generic Radon projections, without taking into account measured intensity. Each digit corresponds to the index of a vertex in Figure 4-9. The first digit corresponds to vertex v_1 of the segment, the second with vertex v_2 , and the third with vertex v_3 | 44 |
| 4.2 | Vertex ordering of the eight possible two segment paths given two generic Radon projections, taking into account measured intensity. Each digit corresponds to the index of a vertex in Figure 4-9. The first digit corresponds to vertex v_1 of the segment, the second with vertex v_2 , and the third with vertex v_3 | 44 |

Chapter 1

Introduction

The process of tomographic imaging is standard in many scientific applications. Probably the largest application of tomographic imaging is in the medical field where computed tomography or CT scans are pervasive. However, these imaging techniques are not without their faults. CT scans require the patient to undergo considerable exposure to x-ray radiation [18][3]. There is considerable research attempting to reduce the amount of radiation exposure to patients [9] as well as reduce the number of projections needed for accurate reconstruction [14].

This thesis will focus on determining the minimum number of projections needed to fully identify a specific class of unknown objects: sheet-like objects with negligible volume. These objects are very sparse in three dimensions, so it is conceivable that they could be identified from a small number of projections. Instead of analyzing and manipulating the large number of samples necessary for traditional tomographic reconstruction techniques, this thesis will address how one might extract information about the unknown object from just a very small number of sample projections; instead of thousands, we will analyze only one, two, or three.

Limiting our object space to a simplified, sparse object will allow us to theoretically reconstruct these objects exactly without the need of filtering or the use of approximations or approximate identities. This restriction can be thought of as an academic exercise to better understand the limits of tomographic imaging and to gain a more fundamental understanding of the Radon transform and the sinogram

themselves.

Restricting our objects to resemble sheets may not be able to directly address the more general problem of decreasing the number of projections needed to image a person in a full body CT scan. However, this theory does have foreseeable applications. While biological samples are not typically sheet-like nor are typically flat or piecewise isometric, many man-made objects are.

Computed tomography is already being used for some commercial freight and airport security to image packages with sheet-like qualities and for explosives detection [11]. However, this imaging technique is not currently used on a large scale because scanning for multiple projections takes time, while adding additional cameras carries considerable cost. If we could harness some tomographic reconstruction techniques to perform reasonable reconstruction with only two or three projections, it might be possible to bring truly three dimensional screening into the mainstream.

A perhaps more direct application for the theory derived in this paper is to characterize three dimensional folded structures. Most folded structures on a large scale can be measured directly, so trying to characterize them using tomographic imaging might not improve on existing techniques. However, more and more research is being devoted to manufacturing and folding [13] three dimensional objects on the micro and nano scales.

Current imaging techniques to characterize three dimensional micro-surfaces such as electron beam microscopy and interferometric techniques are not suitable for truly three dimensional objects with many layers. When trying to characterize multilayered objects (like a crumpled ball of paper [5]) a better technique is to use tomography. Currently, folded micro and nano-surfaces are characterized by fairly simple geometry for which more traditional imaging techniques can be applied. However, when more complicated and layered objects begin to be manufactured, tomographic imaging will play a more significant role, and the theory developed in this paper can be put to use directly.

This thesis is organized into three sections. The first section address traditional methods of tomographic reconstruction. It briefly reviews the Radon transform,

summarizes methods of filtered backprojection, and mentions the use of compressive sensing to obtain better tomographic reconstructions for sparse objects in the traditional tomographic framework. The second section derives a model for representing surface-like objects as a composition of infinite attenuation values. The third section comprises the majority of the thesis. It discusses identification algorithms for increasingly complex surface objects using a minimal number of projections with different amounts of prior knowledge.

Chapter 2

Tomography

Tomography is traditionally used to reconstruct three dimensional objects with finite density from imaged projections of the object. In general, this process requires the observer to sample a large number of projections of the object. Medical imaging for CT scans for example traditionally require projection measurements on the order of 10,000 or more for a reasonable reconstruction [3]. Compressive sensing minimizing total variation of the object can substantially decrease the number of required projections, but still require hundreds of projection measurements depending on the object. We will summarize traditional tomographic reconstruction methods in this section.

2.1 Radon Transform

The general definition of a Radon transform in \mathbb{R}^n is given as the integration of the attenuation function $\mu(\mathbf{x})$ over hyperplanes $\langle \mathbf{x}, \boldsymbol{\theta} \rangle = s$ parameterized by a direction $\boldsymbol{\theta} \in S^{n-1}$ and distance from the origin $s \in \mathbb{R}$:

$$\mathcal{R}\mu(\boldsymbol{\theta}, s) = \int_{\langle \mathbf{x}, \boldsymbol{\theta} \rangle = s} \mu(\mathbf{x}) d\mathbf{x} \quad (2.1)$$

For a given direction $\boldsymbol{\theta}$, the Radon transform gives a one dimensional function of s representing the integration of the space over a hyperplane perpendicular to $\boldsymbol{\theta}$. We will denote a *Radon projection* as the Radon transform constrained to a specific

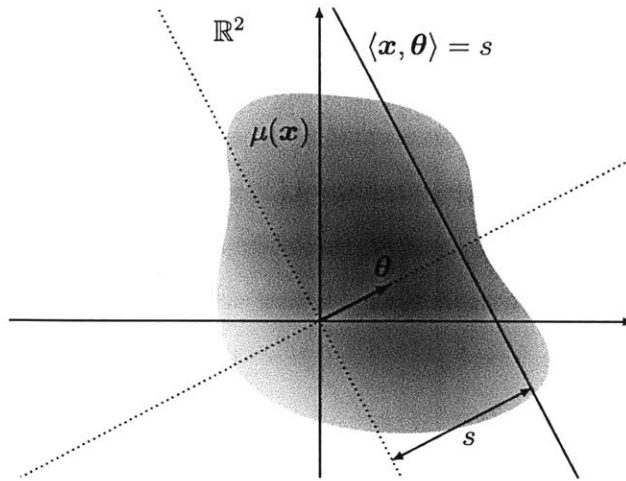


Figure 2-1: Geometry of the Radon transform.

direction $\boldsymbol{\theta}$ as:

$$\mathcal{R}_{\boldsymbol{\theta}}\mu(s) = \mathcal{R}\mu(\boldsymbol{\theta}, s) \quad (2.2)$$

2.2 Fourier Slice Theorem

Radon transforms have the nice property that they are related to the Fourier transform in a specific way. Recall the definition of the Fourier transform of scalar function $f : \mathbb{R}^n \mapsto \mathbb{R}$ as:

$$\mathcal{F}f(\boldsymbol{\xi}) = \int_{\mathbb{R}^n} f(\mathbf{x}) \exp\{-2\pi i \langle \mathbf{x}, \boldsymbol{\xi} \rangle\} d\mathbf{x} \quad (2.3)$$

The *Fourier Slice Theorem* then states, if f is integrable on \mathbb{R}^n and if $\boldsymbol{\theta}$ is a unit vector, then:

$$\mathcal{F}\mathcal{R}_{\boldsymbol{\theta}}f(s) = \mathcal{F}f(s\boldsymbol{\theta}) \quad (2.4)$$

A derivation of this relation found in [16] is as follows:

$$\mathcal{F}f(s\boldsymbol{\theta}) = \int_{\mathbb{R}^n} f(\mathbf{x}) \exp\{-2\pi i \langle \mathbf{x}, s\boldsymbol{\theta} \rangle\} d\mathbf{x} \quad (2.5)$$

$$= \int_{\mathbb{R}} \left[\int_{\langle \boldsymbol{\theta}, \mathbf{x} \rangle = p} f(\mathbf{x}) \exp\{-2\pi i \langle \mathbf{x}, s\boldsymbol{\theta} \rangle\} d\mathbf{x} \right] dp \quad (2.6)$$

$$= \int_{\mathbb{R}} \left[\int_{\langle \boldsymbol{\theta}, \mathbf{x} \rangle = p} f(\mathbf{x}) d\mathbf{x} \right] \exp\{-2\pi i sp\} dp \quad (2.7)$$

$$= \int_{\mathbb{R}} \mathcal{R}_{\boldsymbol{\theta}} f(p) \exp\{-2\pi i sp\} dp \quad (2.8)$$

$$= \mathcal{F}\mathcal{R}_{\boldsymbol{\theta}} f(s) \quad (2.9)$$

Essentially, the Fourier Slice Theorem says that the Fourier transform of the Radon projection of an object is equal to the object's Fourier transform evaluated on the line perpendicular to that projection [10]. The basis of reconstructions and approximate reconstructions of Radon transforms extending from this theorem are based on a process called *filtered backprojection*.

2.3 Filtered Backprojection

If we smear a Radon projection back across the original object space, we get what we call a *backprojection*:

$$\mathcal{R}_{\boldsymbol{\theta}}^{\#} g(\mathbf{x}) = g(\boldsymbol{\theta}, \langle \mathbf{x}, \boldsymbol{\theta} \rangle) \quad (2.10)$$

The *averaged backprojection* is given by integrating these backprojections over all backprojections:

$$\mathcal{R}^{\#} g(\mathbf{x}) = \int_{S^{n-1}} g(\boldsymbol{\theta}, \langle \mathbf{x}, \boldsymbol{\theta} \rangle) d\boldsymbol{\theta} \quad (2.11)$$

where S^{n-1} represents the set of all unit vectors in \mathbb{R}^n . The averaged backprojection of the Radon transform of an object yields a blurred version of the original object

[17] given by:

$$\mathcal{R}^\# \mathcal{R}f = T * f \quad (2.12)$$

$$T(\mathbf{x}) = |S^{n-2}| \frac{1}{\|\mathbf{x}\|} = \frac{2\pi^{n/2}}{\Gamma(n/2)} \frac{1}{\|\mathbf{x}\|} \quad (2.13)$$

The blurring due to the convolution with $T(\mathbf{x})$ is quite significant. In order to perfectly reconstruct the original object, we can filter the Radon transform before taking the averaged backprojection.

$$\mathcal{R}^\#(w) * f = \mathcal{R}^\#(w * \mathcal{R}f) \quad (2.14)$$

Filtering the Radon transform with functions w with the property that $\mathcal{R}^\#(w) * f = f$ will result in a perfect reconstruction. Theoretically, such functions exist [16], with $\mathcal{R}^\#(w)$ approximating a delta function, yielding an exact inversion formula for the Radon transform. However, in practice, noise and discrete sampling often make other filters [1] which do not represent exact inversion preferable for the approximate reconstruction of objects, depending on the signal to noise ratio and the object type. Reconstructed tomographic images can also be further enhanced using post reconstruction filtering [4].

2.4 X-ray transform

A similar transform to the Radon transform is the *x-ray transform* which integrates the attenuation function over lines L instead of hyperplanes:

$$\mathcal{X}\mu(\mathbf{x}, \boldsymbol{\theta}) = \int_{\mathbf{x} \in L} \mu(\mathbf{x}) d\mathbf{x} = \int_{-\infty}^{\infty} \mu(\mathbf{x} + t\boldsymbol{\theta}) dt \quad (2.15)$$

Note that in two dimensional space (\mathbb{R}^2), hyperplanes are lines, and thus the Radon transform and the x-ray transform correspond to the same transform. Relationships [8][19] between these transforms have been thoroughly studied in many dimensions. While the Radon transform may be more convenient from a reconstruction point of view, due to its special relationship to the Fourier transform, the x-ray

transform is considerably more practical in terms of experimental measurement. The reason lies in the following property of light.

2.5 Beer-Lambert Law

Before continuing further, we should introduce the Beer-Lambert Law. Up until now, we have talked about taking Radon and x-ray projections without putting these mathematical definitions into a physical framework. The physical justification for studying these transforms is that we can measure something similar to a line integral of attenuation by illuminating an object with a known light source and taking a picture of its shadow. The Beer-Lambert Law relates the input light intensity I_0 to the output light intensity I by way of a line integral through the attenuation function [12].

$$I = I_0 \exp \left\{ - \int_L \mu(\mathbf{x}) d\mathbf{x} \right\} \quad (2.16)$$

Solving for the line integral yields:

$$- \ln \left| \frac{I}{I_0} \right| = \int_{\mathbf{x} \in L} \mu(\mathbf{x}) d\mathbf{x} = \mathcal{X}\mu(\mathbf{x}, \boldsymbol{\theta}) \quad (2.17)$$

This equations gives us a physical justification for studying x-ray and Radon transforms and a way of measuring them in the real world. In particular, in two dimensions (\mathbb{R}^2),

$$I(\boldsymbol{\theta}, s) = I_0 \exp \{ \mathcal{R}\mu(\boldsymbol{\theta}, s) \} \quad (2.18)$$

2.6 Two Dimensional Radon Transforms

As we have seen, two dimensional Radon transforms are particularly special because they correspond to x-ray transforms and their Radon projections can be measured directly in the physical world. Individual Radon projections in three dimensions

and higher do not have this correspondence, so additional mathematical complexity is involved in the conversion between x-ray projections to Radon projections. In a typical CT scanning device, cone-beam or fan projections are measured which are effectively reorganizations of x-ray projection data.

In this thesis, we will focus our attention on two dimensional Radon transforms and their inversion. Our object will live in \mathbb{R}^2 , be a one dimensional curve embedded in two dimensions, and Radon projections will integrate over lines. All of our analysis should be applicable to objects in three dimensions by analyzing the three dimensional volume in two dimensional slices.

In two dimensional space (\mathbb{R}^2) we can write our Radon transform as:

$$\mathcal{R}\mu(\theta, s) = \mathcal{R}\mu(\boldsymbol{\theta}, s) = \int_{\langle \mathbf{x}, \boldsymbol{\theta} \rangle = s} \mu(\mathbf{x}) d\mathbf{x} \quad (2.19)$$

Where $\boldsymbol{\theta} = (\cos \theta, \sin \theta)$ and $\mathbf{x} \in \mathbb{R}^2$.

Two useful properties of two dimensional Radon projections is that they are even functions with respect to θ and s :

$$\mathcal{R}\mu(-\theta, -s) = \mathcal{R}\mu(\theta, s) \quad (2.20)$$

and they are periodic with a period of 2π :

$$\mathcal{R}\mu(\theta, s) = \mathcal{R}\mu(\theta + 2\pi, s) \quad (2.21)$$

These two properties mean that the two dimensional Radon transform of the entire θ domain can be found from any interval of size π . Thus, when we plot two dimensional Radon transforms, we will only plot them on the range from $\theta = [0, \pi)$ as this will be representative of the entire transform.

2.7 Compressive Sensing

When performing tomographic imaging on an object, the above reconstruction methods generally require sampling at the nyquist frequency in order to perform a reasonable reconstruction. In recent years, a sampling and processing technique called compressive sensing [7] has been studied to exploit the fact that objects being observed are often sparse in some basis. By assuming your unknown object is sparse in some basis, one can use linear programming to search for a reconstruction solution that takes in to account this sparsity to provide a more accurate reconstruction for objects that are indeed sparse in that basis. Compressive sensing is currently being investigated for use in MR imaging [15], image processing [2], and other signal reconstruction applications [6]. Similar to the compressive sensing algorithm, we will assume our object has certain characteristics and exploit these characteristics to search for a reconstruction solution given fewer measurements than would classically be needed.

Chapter 3

Surface Attenuation Model

We typically model the attenuation of light through an object by assigning a finite attenuation coefficient per unit length to every point in space. To image a projection of the object, we then integrate this attenuation function onto the projected surface. Sheet-like surfaces have zero volume, so in order to adhere to this model, we will have to assign infinite values to points on the surface. In this section, we propose an attenuation model for thin surfaces by composing them from delta functions.

3.1 Hypersurfaces

In geometry, a *manifold* is a simply connected topological space that locally resembles the Euclidean space of a specific dimension at every point. For example, a one-dimensional manifold looks locally like a line at every point, while a two-dimensional manifold looks locally like a plane at every point. We will denote an n -dimensional manifold as an n -manifold, and any real Euclidean n -dimensional space as \mathbb{R}^n . We will also denote \mathbb{R}^1 as \mathbb{R} . Furthermore, let S^{n-1} represent the unit n -sphere: the set of all unit vectors in \mathbb{R}^n . S^{n-1} is clearly a manifold of dimension $n - 1$ as it represents the surface boundary of the unit n -ball.

A *hypersurface* is a specific type of manifold for which the dimension of the manifold is one less than the dimension of the space in which it is embedded. For example, a piece of paper folded in three dimensions (a 2-manifold embedded in \mathbb{R}^3) would

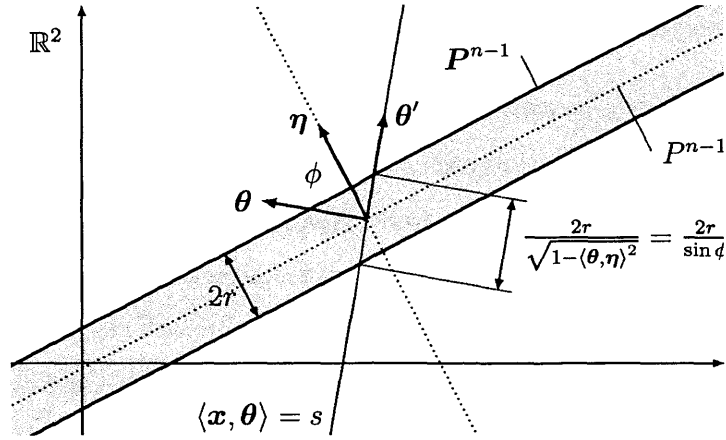


Figure 3-1: Geometry of a line projection $\langle x, \theta \rangle = s$ crossing a hyperplane P^{n-1} of thickness $2r$ in \mathbb{R}^2 at angle ϕ given by $\sqrt{1 - \langle \theta, \eta \rangle^2} = \sin \phi$.

be an example of a hypersurface, while a string twisting around in three-dimensions (a 1-manifold embedded in \mathbb{R}^3) would not. We choose to restrict our analysis to hypersurfaces because they possess two properties:

1. The Lebesgue measure on \mathbb{R}^n of a hypersurface is zero. In other words, the hypersurface has zero volume.
2. The Lebesgue measure on \mathbb{R}^{n-1} of the projection of a hypersurface onto \mathbb{R}^{n-1} can be nonzero. In other words, the hypersurface has nonzero surface area.

Modeling the attenuation function for a hypersurface is not obvious. If the hypersurface is infinitely thin, then its attenuation coefficient per unit length at each point on the surface must also in some sense be infinite in order to have nonzero attenuation across the hypersurface. We will derive the form of this attenuation coefficient based on a limiting case.

3.2 Attenuation Function of Hyperplanes

Before we try to define the attenuation function for a general hypersurface, let us address the simpler problem of modeling a *hyperplane*. A hyperplane is a flat hypersurface with constant surface normal everywhere, extending infinitely in all directions.

The following set describes a hyperplane with surface normal in the direction $\boldsymbol{\eta} \in S^{n-1}$ and distance $\sigma \in \mathbb{R}$ from the origin:

$$P^{n-1} = \{\mathbf{x} \in \mathbb{R}^n : \langle \mathbf{x}, \boldsymbol{\eta} \rangle = \sigma\} \quad (3.1)$$

where $\langle \mathbf{a}, \mathbf{b} \rangle$ represents the scalar product of vectors \mathbf{a} and \mathbf{b} . Let us give this hyperplane thickness by extending it by a small distance $r \in \mathbb{R}$ in the $\pm\boldsymbol{\eta}$ directions. The following set describes our new thickened hyperplane:

$$P^{n-1} = \{\mathbf{x} \in \mathbb{R}^n : |\langle \mathbf{x}, \boldsymbol{\eta} \rangle - \sigma| \leq r\} \quad (3.2)$$

Let α represent the total attenuation across this surface in the normal direction, with zero attenuation outside. Then the attenuation per unit length inside the surface would then be $\alpha/2r$. Recall the notation $f : \mathbb{R}^n \rightarrow \mathbb{R}$ defining a function f which maps the space \mathbb{R}^n onto \mathbb{R} . We can write the attenuation function $\mu : \mathbb{R}^n \rightarrow \mathbb{R}$ of our thickened hyperplane as:

$$\mu_P(\mathbf{x}) = \frac{\alpha}{2r} \text{rect} \left(\frac{\langle \mathbf{x}, \boldsymbol{\eta} \rangle - \sigma}{2r} \right) \quad (3.3)$$

where the rectangular function $\text{rect}(x) : \mathbb{R} \mapsto \mathbb{R}$ is defined as:

$$\text{rect}(x) = \begin{cases} 1 & \text{if } |x| \leq \frac{1}{2} \\ 0 & \text{if } |x| > \frac{1}{2} \end{cases} \quad (3.4)$$

To model this attenuation function as an infinitely thin hyperplane, we take the limit as r goes to zero:

$$\mu_P(\mathbf{x}) = \lim_{r \rightarrow 0} \frac{\alpha}{2r} \text{rect} \left(\frac{\langle \mathbf{x}, \boldsymbol{\eta} \rangle - \sigma}{2r} \right) \quad (3.5)$$

Here it will be useful to recall the Dirac delta function, a generalized function satisfying the following two conditions:

$$(I) \quad \delta(x) = 0 \quad \text{when } x \neq 0 \quad (3.6)$$

$$(II) \quad \int_{-\infty}^{\infty} \delta(x) dx = 1 \quad (3.7)$$

The delta function has a number of useful properties. It acts as an identity under convolution:

$$\int_{-\infty}^{\infty} f(x) \delta(x - a) dx = f(a) \quad (3.8)$$

It scales according to:

$$\delta(\alpha x) = \frac{\delta(x)}{|\alpha|} \quad (3.9)$$

Also, any bounded function $\varphi : \mathbb{R} \mapsto \mathbb{R}$ that integrates to 1 from $-\infty$ to ∞ can approximate the delta function by scaling its domain sufficiently while preserving its integral:

$$\delta(x) = \lim_{\varepsilon \rightarrow 0} \frac{1}{\varepsilon} \varphi\left(\frac{x}{\varepsilon}\right) \quad (3.10)$$

Since the rectangular function is bounded and integrates to 1 from $-\infty$ to ∞ , we have:

$$\mu_P(\mathbf{x}) = \alpha \delta(\langle \mathbf{x}, \boldsymbol{\eta} \rangle - \sigma) \quad (3.11)$$

Here we have compressed the volume of the thick hyperplane onto the infinitely thin hyperplane, and in doing so made the attenuation function infinite where nonzero.

3.3 Attenuation Function of Hypersurfaces

The above derivation justifies an attenuation model of an infinitely thin hyperplane as a plane of delta functions. We will extend this model to hypersurfaces by placing a delta function at every point on the hypersurface:

$$\mu_{H^{n-1}}(\mathbf{x}) = \alpha(\mathbf{x}) \int_{\mathbf{p} \in H^{n-1}} \delta(\mathbf{x} - \mathbf{p}) \quad (3.12)$$

Chapter 4

Identification of Surface Objects

Traditional tomography generally requires a large number of projections to achieve an accurate reconstruction. In this section, we will show that certain types of objects, specifically surface objects, can be fully reconstructed from as few as two projections given that each projection can be measured with perfect resolution. We will restrict our analysis to surface objects described by one dimensional curves in two dimensions.

In this chapter, we will restrict our analysis to identifying an unknown object provided a minimal number of *perfect projections*. A perfect projection can be thought of as the exact Radon transform of the object restricted to a specific direction. We assume infinite spatial resolution as well as perfect intensity measurement accuracy. This section seeks to explore the limits on the number of projections needed to identify certain objects without the presence of noise or other physical restrictions.

4.1 Identification of a Point Object

Let us begin our identification process with the simplest of objects: the point object. In general, our point will be described by three parameters: a position in \mathbb{R}^2 specified by $\mathbf{p} = (x_p, y_p)$ and an attenuation factor α_p . We can also represent the position coordinates of \mathbf{p} in terms of polar parameters $r_p = \sqrt{x_p^2 + y_p^2}$ and $\phi_p = \text{atan2}(y_p, x_p)$:

$$\mathbf{p} = (x_p, y_p) = (r_p \cos \phi_p, r_p \sin \phi_p) = r_p \hat{\phi}_p \quad (4.1)$$

where $\hat{\phi}_p = (\cos \phi_p, \sin \phi_p)$ and the function $\text{atan2} : \mathbb{R}, \mathbb{R} \mapsto (-\pi, \pi]$ extends the range of the typical function $\arctan : \mathbb{R} \mapsto (-\pi/2, \pi/2)$ according to:

$$\text{atan2}(y, x) = \begin{cases} \arctan\left(\frac{y}{x}\right) & x > 0 \\ \pi + \arctan\left(\frac{y}{x}\right) & y \geq 0, x < 0 \\ -\pi + \arctan\left(\frac{y}{x}\right) & y < 0, x < 0 \\ \frac{\pi}{2} & y > 0, x = 0 \\ -\frac{\pi}{2} & y < 0, x = 0 \\ \text{undefined} & y = 0, x = 0 \end{cases} \quad (4.2)$$

The attenuation function for our point object is then given by:

$$\mu_p(x, y) = \alpha_p \delta(x - x_p) \delta(y - y_p) = \alpha_p \delta(\mathbf{x} - \mathbf{p}) \quad (4.3)$$

Recall in \mathbb{R}^2 , the Radon transform for our point object will be given by:

$$\mathcal{R}\mu_p(\boldsymbol{\theta}, s) = \alpha_p \int_{\langle \mathbf{x}, \boldsymbol{\theta} \rangle = s} \delta(\mathbf{x} - \mathbf{p}) d\mathbf{x} \quad (4.4)$$

for $\boldsymbol{\theta} = (\cos \theta, \sin \theta)$. Simplifying this equation with the definitions of \mathbf{p} and $\boldsymbol{\theta}$ yields:

$$\mathcal{R}\mu_p(\boldsymbol{\theta}, s) = \alpha_p \delta(s - \langle \mathbf{p}, \boldsymbol{\theta} \rangle) \quad (4.5)$$

$$\mathcal{R}\mu_p(\theta, s) = \alpha_p \delta(s - r_p(\cos \theta \cos \phi_p + \sin \theta \sin \phi_p)) \quad (4.6)$$

$$\mathcal{R}\mu_p(\theta, s) = \alpha_p \delta(s - r_p \cos(\theta - \phi_p)) \quad (4.7)$$

Below is a plot of locations where the delta function of the point's Radon transform is nonzero. It represents a single sinusoid in Radon space. This is why two dimensional radon transforms plotted with s and θ as axes are sometimes called *sinograms*. However, instead of plotting the radon transform rectilinearly as we have done on the sinogram, one can also plot the radon transform in two dimensional space by taking $\boldsymbol{\theta}$ and s to represent polar coordinates in the original object space. Let us transform

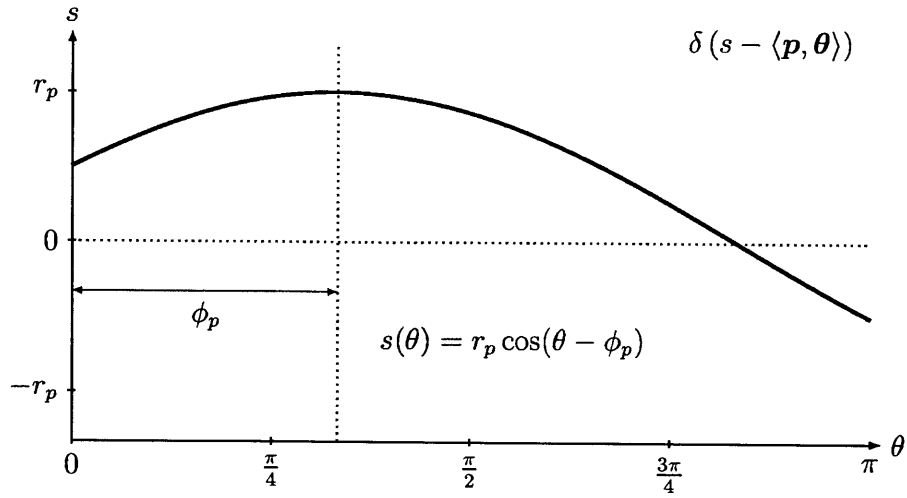


Figure 4-1: Nonzero locations of the Radon transform sinogram of a point in \mathbb{R}^2 .

$$(\boldsymbol{\theta}, s) \rightarrow \mathbf{x} \in \mathbb{R}^2: \quad s = \|\mathbf{x}\| \quad \boldsymbol{\theta} = \frac{\mathbf{x}}{\|\mathbf{x}\|} \quad (4.8)$$

Then for $\delta(s - \langle \mathbf{p}, \boldsymbol{\theta} \rangle)$ to be nonzero:

$$\begin{aligned} \|\mathbf{x}\| &= \left\langle \mathbf{p}, \frac{\mathbf{x}}{\|\mathbf{x}\|} \right\rangle \\ \|\mathbf{x}\|^2 &= \langle \mathbf{p}, \mathbf{x} \rangle \\ \|\mathbf{x}\|^2 - 2\left\langle \mathbf{x}, \frac{\mathbf{p}}{2} \right\rangle + \left\| \frac{\mathbf{p}}{2} \right\|^2 &= \left\| \frac{\mathbf{p}}{2} \right\|^2 \\ \left\langle \mathbf{x} - \frac{\mathbf{p}}{2}, \mathbf{x} - \frac{\mathbf{p}}{2} \right\rangle &= \left\| \frac{\mathbf{p}}{2} \right\|^2 \\ \left\| \mathbf{x} - \frac{\mathbf{p}}{2} \right\|^2 &= \left\| \frac{\mathbf{p}}{2} \right\|^2 \end{aligned}$$

And:

$$\delta(s - \langle \mathbf{p}, \boldsymbol{\theta} \rangle) = \delta\left(\left\| \frac{\mathbf{p}}{2} \right\|^2 - \left\| \mathbf{x} - \frac{\mathbf{p}}{2} \right\|^2\right) \quad (4.9)$$

In other words, the Radon transform maps each point \mathbf{p} in the object space onto the surface of a sphere in Radon space. The line running from the origin to \mathbf{p} constructs a diameter of the sphere. In \mathbb{R}^2 , each point maps to a circle. For convenience and for comparison with sinograms, we will call plots of the Radon transform in this spacial domain *circlegrams*. We clearly observe that the signature of a point object in Radon space is a sinusoid with a period of 2π or a circle containing the origin, depending on

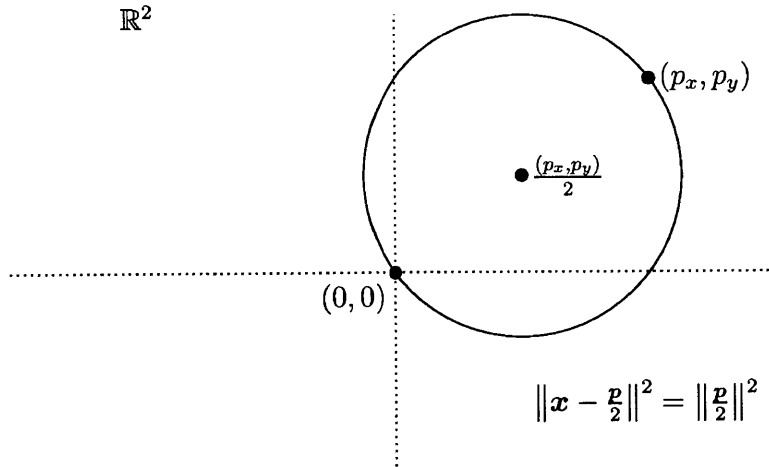


Figure 4-2: Nonzero locations of the Radon transform circlegram of a point in \mathbb{R}^2 .

how you plot the Radon transform. One can uniquely specify a sinusoid in a sinogram with two points on the sinusoid. For the circlegram, three points are necessary to uniquely specify a circle. However, we notice that the origin is necessarily contained on the circle, so we only need to specify two additional points on the circle to uniquely specify its location. Thus, we should be able to identify the location of the point object simply from two distinct Radon projections.

For example, given distinct projection angles $\theta_1, \theta_2 \in [0, \pi)$, suppose we observe zero integrated attenuation everywhere except the points s_1 and s_2 respectively where infinite integral attenuation is observed. Then each nonzero projection must satisfy Equation 4.9:

$$\left(s_i \cos \theta_i - \frac{p_x}{2}\right)^2 + \left(s_i \sin \theta_i - \frac{p_y}{2}\right)^2 = \frac{(p_x^2 + p_y^2)^2}{2} \quad (4.10)$$

Then after simplification, the location of the point object (p_x, p_y) will be given by the solution to the following linear system:

$$\begin{bmatrix} s_1 \cos \theta_1 & s_1 \sin \theta_1 \\ s_2 \cos \theta_2 & s_2 \sin \theta_2 \end{bmatrix} \begin{bmatrix} p_x \\ p_y \end{bmatrix} = \begin{bmatrix} s_1^2 \\ s_2^2 \end{bmatrix} \quad (4.11)$$

Note that the determinant of this system is zero when:

$$s_1 s_2 (\sin \theta_2 \cos \theta_1 - \cos \theta_2 \sin \theta_1) = s_1 s_2 \sin(\theta_2 - \theta_1) = 0 \quad (4.12)$$

Since θ_1 and θ_2 are distinct, $\sin(\theta_2 - \theta_1)$ will never be zero for $\theta_1, \theta_2 \in [0, \pi)$. However, if s_1 (or symmetrically s_2) is equal to zero, then \mathbf{p} is perpendicular to $\boldsymbol{\theta}_1$, thus we can solve the following modified linear equation:

$$\begin{bmatrix} \cos \theta_1 & \sin \theta_1 \\ s_2 \cos \theta_2 & s_2 \sin \theta_2 \end{bmatrix} \begin{bmatrix} p_x \\ p_y \end{bmatrix} = \begin{bmatrix} 0 \\ s_2^2 \end{bmatrix} \quad (4.13)$$

Thus, given two distinct projections, we can fully identify a point object's location. However, since it's attenuation is infinite, we cannot determine its attenuation coefficient α_p . As we will see shortly, this will not be the case for one dimensional curves composed of a continuum of points, and we will be able to deduce the attenuation coefficient of the curve via its integrated attenuation.

4.2 Identification of a Line Segment Object

Let us now define a line segment L with constant attenuation coefficient α_L composed of the line segment bounded by vertices $\mathbf{v}_1 = (v_{1x}, v_{1y})$ and $\mathbf{v}_2 = (v_{2x}, v_{2y})$. The set L can be formally defined as:

$$L = \{\mathbf{x} \in \mathbb{R}^2 : \mathbf{x} = \mathbf{v}_1 + t(\mathbf{v}_2 - \mathbf{v}_1) \quad \forall t \in [0, 1]\} \quad (4.14)$$

The attenuation function for our line object can be given as an integral of delta functions:

$$\mu_L(\mathbf{x}) = \alpha_L \int_{\mathbf{p} \in L} \delta(\mathbf{x} - \mathbf{p}) = \alpha_L \int_0^{\|\mathbf{v}_2 - \mathbf{v}_1\|} \delta\left(\mathbf{x} - \left(\mathbf{v}_1 + t \frac{\mathbf{v}_2 - \mathbf{v}_1}{\|\mathbf{v}_2 - \mathbf{v}_1\|}\right)\right) dt \quad (4.15)$$

Then the Radon transform of L can be written as:

$$\mathcal{R}\mu_L(\boldsymbol{\theta}, s) = \alpha_L \int_{\langle \mathbf{x}, \boldsymbol{\theta} \rangle = s} \int_0^{\|\mathbf{v}_2 - \mathbf{v}_1\|} \delta \left(\mathbf{x} - \left(\mathbf{v}_1 + t \frac{\mathbf{v}_2 - \mathbf{v}_1}{\|\mathbf{v}_2 - \mathbf{v}_1\|} \right) \right) dt d\mathbf{x} \quad (4.16)$$

$$\mathcal{R}\mu_L(\boldsymbol{\theta}, s) = \alpha_L \int_0^{\|\mathbf{v}_2 - \mathbf{v}_1\|} \delta \left(s - \left\langle \mathbf{v}_1 + t \frac{\mathbf{v}_2 - \mathbf{v}_1}{\|\mathbf{v}_2 - \mathbf{v}_1\|}, \boldsymbol{\theta} \right\rangle \right) dt \quad (4.17)$$

$$\mathcal{R}\mu_L(\boldsymbol{\theta}, s) = \alpha_L \int_0^{\|\mathbf{v}_2 - \mathbf{v}_1\|} \delta \left(s - \langle \mathbf{v}_1, \boldsymbol{\theta} \rangle + t \left\langle \frac{\mathbf{v}_2 - \mathbf{v}_1}{\|\mathbf{v}_2 - \mathbf{v}_1\|}, \boldsymbol{\theta} \right\rangle \right) dt \quad (4.18)$$

$$\mathcal{R}\mu_L(\boldsymbol{\theta}, s) = \frac{\alpha_L}{\left| \left\langle \frac{\mathbf{v}_2 - \mathbf{v}_1}{\|\mathbf{v}_2 - \mathbf{v}_1\|}, \boldsymbol{\theta} \right\rangle \right|} \int_0^{\|\mathbf{v}_2 - \mathbf{v}_1\|} \delta \left(\frac{s - \langle \mathbf{v}_1, \boldsymbol{\theta} \rangle}{\left\langle \frac{\mathbf{v}_2 - \mathbf{v}_1}{\|\mathbf{v}_2 - \mathbf{v}_1\|}, \boldsymbol{\theta} \right\rangle} + t \right) dt \quad (4.19)$$

Now we can represent this integral of delta functions as a rectangular function via the relation:

$$\text{rect} \left(\frac{x - c}{a} \right) = \int_{c - \frac{a}{2}}^{c + \frac{a}{2}} \delta(x + t) dt \quad (4.20)$$

Taking $a = \|\mathbf{v}_2 - \mathbf{v}_1\|$ and $c = \|\mathbf{v}_2 - \mathbf{v}_1\|/2$, the Radon transform for the line segment object L becomes:

$$\mathcal{R}\mu_L(\boldsymbol{\theta}, s) = \frac{\alpha_L}{\left| \left\langle \frac{\mathbf{v}_2 - \mathbf{v}_1}{\|\mathbf{v}_2 - \mathbf{v}_1\|}, \boldsymbol{\theta} \right\rangle \right|} \text{rect} \left(\frac{s - \langle \mathbf{v}_2 + \mathbf{v}_1, \boldsymbol{\theta} \rangle / 2}{\langle \mathbf{v}_2 - \mathbf{v}_1, \boldsymbol{\theta} \rangle} \right) \quad (4.21)$$

Note in the limit as $\langle \mathbf{v}_2 - \mathbf{v}_1, \boldsymbol{\theta} \rangle$ goes to zero, this Radon transform becomes a delta function, but is finite when $\langle \mathbf{v}_2 - \mathbf{v}_1, \boldsymbol{\theta} \rangle \neq 0$. Note also that the magnitude of the Radon transform takes on values between α_L and infinity. For simplicity, let us define vectors $\mathbf{v}_\Delta = \mathbf{v}_2 - \mathbf{v}_1$ and $\mathbf{v}_\Sigma = (\mathbf{v}_2 + \mathbf{v}_1)/2$. Then the line segment Radon transform becomes:

$$\mathcal{R}\mu_L(\boldsymbol{\theta}, s) = \frac{\alpha_L \|\mathbf{v}_\Delta\|}{|\langle \mathbf{v}_\Delta, \boldsymbol{\theta} \rangle|} \text{rect} \left(\frac{s - \langle \mathbf{v}_\Sigma, \boldsymbol{\theta} \rangle}{\langle \mathbf{v}_\Delta, \boldsymbol{\theta} \rangle} \right) \quad (4.22)$$

In the physical world, we will measure an intensity change according to the Beer-

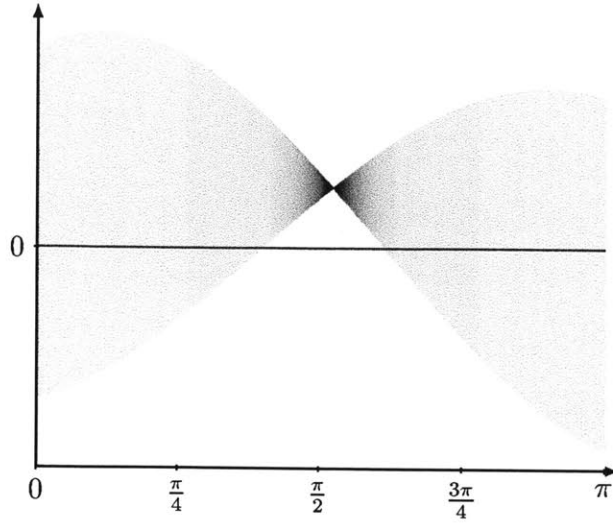


Figure 4-3: Intensity converted Radon transform sinogram of generic line segment L with $\alpha = 0.2$.

Lambert Law (Equation 2.16). In this case, we will measure a finite intensity given by:

$$I(\boldsymbol{\theta}, s) = I_0 \exp \left\{ \frac{\alpha_L \|\mathbf{v}_\Delta\|}{|\langle \mathbf{v}_\Delta, \boldsymbol{\theta} \rangle|} \text{rect} \left(\frac{s - \langle \mathbf{v}_\Sigma, \boldsymbol{\theta} \rangle}{\langle \mathbf{v}_\Delta, \boldsymbol{\theta} \rangle} \right) \right\} \quad (4.23)$$

This measured intensity passing through the line segment will range from 0 when the integral attenuation is infinite, to $I_0 e^{\alpha_L}$ when the line runs parallel to $\boldsymbol{\theta}$. Figures 4-3 and 4-4 show plots of a sinogram and circlegram respectively of measured intensity for a generic line for $\alpha_L = 0.2$, with black representing zero transmitted intensity and white being unattenuated transmitted intensity I_0 .

Note that the Radon transform of the line segment covers in a sense the union of the Radon transforms of the individual points that make up the segment. Figure 4-5 shows circles corresponding to ten different points on the generic line segment L .

What is the minimum number of projections required to perfectly identify a generic line segment? We will analyze identification using first two distinct projections and three distinct projections respectively.

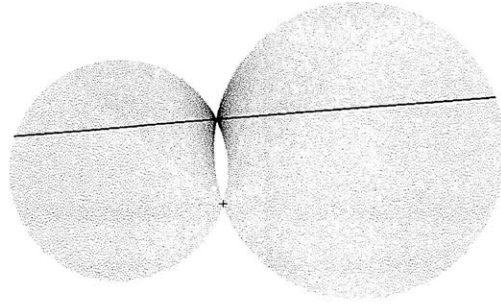


Figure 4-4: Intensity converted Radon transform circlegram of generic line segment L with $\alpha = 0.2$. A “+” marks the origin, with L drawn in black.

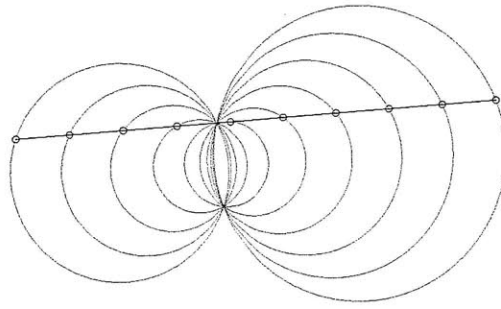


Figure 4-5: Radon transform circlegram for ten evenly spaced points of generic line segment L .

4.2.1 Two Projections

As with the point object, one might expect to be able to identify a line segment from two distinct projections alone. Let us analyze a pair of distinct projections, $\theta_1, \theta_2 \in [0, \pi)$. As long as $\langle \mathbf{v}_\Delta, \boldsymbol{\theta}_i \rangle \neq 0$, for each $\boldsymbol{\theta}_i = (\cos \theta_i, \sin \theta_i)$, each projection will look like a rectangular function that can be characterized by three parameters: its center c_i , its width w_i , and its height (measured intensity) I_i . These three parameters will be functions of angle given by:

$$c_i(\boldsymbol{\theta}_i) = \langle \mathbf{v}_\Sigma, \boldsymbol{\theta}_i \rangle \quad (4.24)$$

$$w_i(\boldsymbol{\theta}_i) = |\langle \mathbf{v}_\Delta, \boldsymbol{\theta}_i \rangle| \quad (4.25)$$

$$I_i(\theta_i) = I_0 \exp \left\{ \frac{\alpha_L \|\mathbf{v}_\Delta\|}{|\langle \mathbf{v}_\Delta, \boldsymbol{\theta}_i \rangle|} \right\} \quad (4.26)$$

For two projections, the equations for c_1 and c_2 fully define the location of the sum of the vertices \mathbf{v}_Σ given by the linear system:

$$\begin{bmatrix} \cos \theta_1 & \sin \theta_1 \\ \cos \theta_2 & \sin \theta_2 \end{bmatrix} \begin{bmatrix} v_{\Sigma x} \\ v_{\Sigma y} \end{bmatrix} = \begin{bmatrix} c_1 \\ c_2 \end{bmatrix} \quad (4.27)$$

However, the equations for w_1 and w_2 do not fully define \mathbf{v}_Δ because of the non-linear absolute value. Four possible systems exist yielding four different sets of answers:

$$\begin{bmatrix} \cos \theta_1 & \sin \theta_1 \\ \cos \theta_2 & \sin \theta_2 \end{bmatrix} \begin{bmatrix} v_{\Delta x} \\ v_{\Delta y} \end{bmatrix} = \begin{bmatrix} \pm w_1 \\ \pm w_2 \end{bmatrix} \quad (4.28)$$

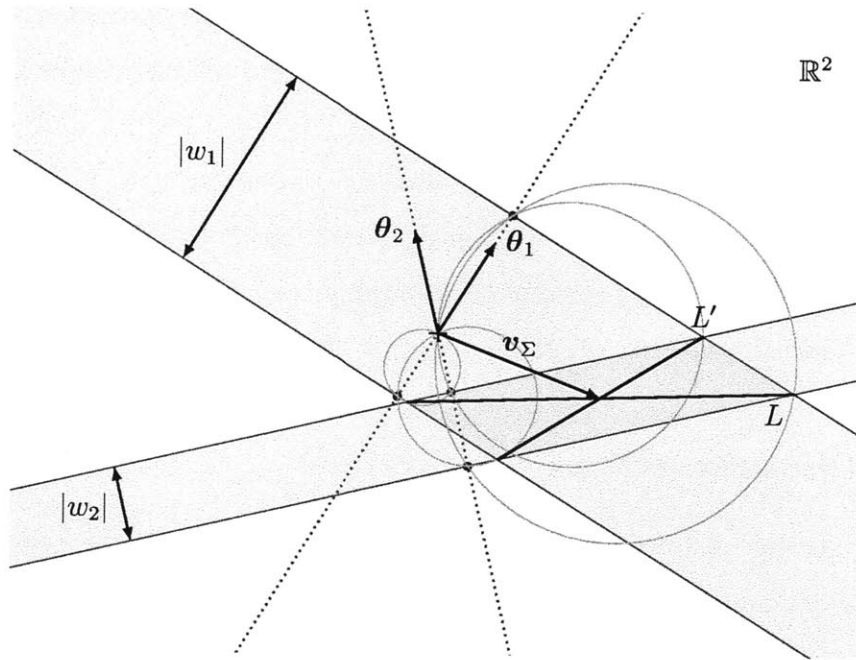


Figure 4-6: Backprojections and two possible circlegrams for one pair of projections of a unknown line segment object, either L or L' .

The four solutions $(v_{\Delta x}, v_{\Delta y})_i$ comprise two different pairs of solutions that are negatives of each other: one pair $\mathbf{v}_{\Delta a} = -\mathbf{v}_{\Delta b}$ for which w_1/w_2 is positive, and

another pair $\mathbf{v}_{\Delta c} = -\mathbf{v}_{\Delta d}$ for which w_1/w_2 is negative. Figure 4-6 shows a plot of the ambiguity of these two solutions. The backprojections formed by the two observed widths w_1 and w_2 smeared back across the object space form a parallelogram in which the line segment can possibly reside, the line segment existing in either diagonal of the parallelogram.

The last two equations (4.26) for measured intensity are actually the same relation for the quantity $\alpha_L \|\mathbf{v}_\Delta\|$ when combined with the width measurements:

$$\alpha_L \|\mathbf{v}_\Delta\| = |\langle \mathbf{v}_\Delta, \boldsymbol{\theta}_i \rangle| \ln \left\{ \frac{I_i(\boldsymbol{\theta}_i)}{I_0} \right\} = w_i(\boldsymbol{\theta}_i) \ln \left\{ \frac{I_i(\boldsymbol{\theta}_i)}{I_0} \right\} \quad (4.29)$$

If we have prior knowledge of α_L , and our two measured projection angles are not perpendicular, we can resolve the ambiguity between the two parallelogram diagonals by having an equation for the diagonal's length $\|\mathbf{v}_\Delta\|$. If the two projection angles are perpendicular, the parallelogram would become a rectangle with two diagonals of identical length, and distinction between the two would not be possible given the above equations.

To summarize identification from two distinct projections, it is not possible to resolve a binary ambiguity without additional information. If the value of α_L is known, identification is possible provided that the two projections are not perpendicular and $\langle \mathbf{v}_\Delta, \boldsymbol{\theta}_i \rangle \neq 0$ for each $\boldsymbol{\theta}_i = (\cos \theta_i, \sin \theta_i)$.

4.2.2 Three Projections

Measuring another distinct projection in addition to our original two projections will yield three more equations: one each for center, width, and height (measured intensity) provided again that $\langle \mathbf{v}_\Delta, \boldsymbol{\theta}_3 \rangle \neq 0$. The equation for center is redundant as the center equations for the first two projections fully define \mathbf{v}_Σ . Similarly, all three equations for measured intensity identically yield the same relation for the value $\alpha_L \|\mathbf{v}_\Delta\|$.

However, the additional equation for width $w_3(\boldsymbol{\theta}_3) = |\langle \mathbf{v}_\Delta, \boldsymbol{\theta}_3 \rangle|$ will resolve the ambiguity for \mathbf{v}_Δ . By plugging in each of the four possible solutions of $\mathbf{v}_{\Delta i}$ into

this third equation's right side, only one will evaluate to the correct measured w_3 (call it $\mathbf{v}_{\Delta a}$). A solution must exist from our presumption that the line segment exists. We must now prove uniqueness of this solution. If the solution exists among the possible solutions, one of the possible solutions must also be its negative (call it $\mathbf{v}_{\Delta b}$). $\mathbf{v}_{\Delta a} \neq \mathbf{v}_{\Delta b} \neq \mathbf{0}$ based on our assumption that $\langle \mathbf{v}_{\Delta}, \boldsymbol{\theta}_i \rangle \neq 0$. Furthermore, $\mathbf{v}_{\Delta a} \neq \mathbf{v}_{\Delta c} \neq \mathbf{v}_{\Delta d}$ because each $\boldsymbol{\theta}_i$ is a distinct projection angle.

With this third projection, \mathbf{v}_{Δ} and \mathbf{v}_{Σ} are both fully defined and unique. This also means that \mathbf{v}_1 and \mathbf{v}_2 can also be fully recovered from the linear system:

$$\begin{bmatrix} -1 & 1 & 0 & 0 \\ 1 & 1 & 0 & 0 \\ 0 & 0 & -1/2 & 1/2 \\ 0 & 0 & 1/2 & 1/2 \end{bmatrix} \begin{bmatrix} v_{1x} \\ v_{2x} \\ v_{1y} \\ v_{2y} \end{bmatrix} = \begin{bmatrix} v_{\Delta x} \\ v_{\Delta y} \\ v_{\Sigma x} \\ v_{\Sigma y} \end{bmatrix} \quad (4.30)$$

Furthermore, $\|\mathbf{v}_{\Delta}\|$ will be known, so α_L can be readily derived from any one of the measured intensity equations.

To summarize, it is possible to fully identify the location $(\mathbf{v}_1, \mathbf{v}_2)$ and attenuation α_L of an unknown line segment object from three distinct projections.

4.3 Identification of Two Connected Line Segments

Let us now consider the identification of two connected line segments; two line segments sharing a vertex. This object is fully defined by its three vertices $(\mathbf{v}_1, \mathbf{v}_2, \mathbf{v}_3)$ and its two attenuation coefficients (α_1, α_2) corresponding to segments $(\mathbf{v}_1, \mathbf{v}_2)$ and $(\mathbf{v}_2, \mathbf{v}_3)$ respectively. This object is simply the superposition of two line objects as described in the previous section. However, the presence of an additional line segment raises issues of ambiguity as to how the object's three vertices are connected, and which vertices are observed at each discontinuity in the Radon transform. Again, for simplicity, let us define the following values:

$$\mathbf{v}_{\Delta 1} = \mathbf{v}_2 - \mathbf{v}_1 \quad \mathbf{v}_{\Delta 2} = \mathbf{v}_3 - \mathbf{v}_2 \quad (4.31)$$

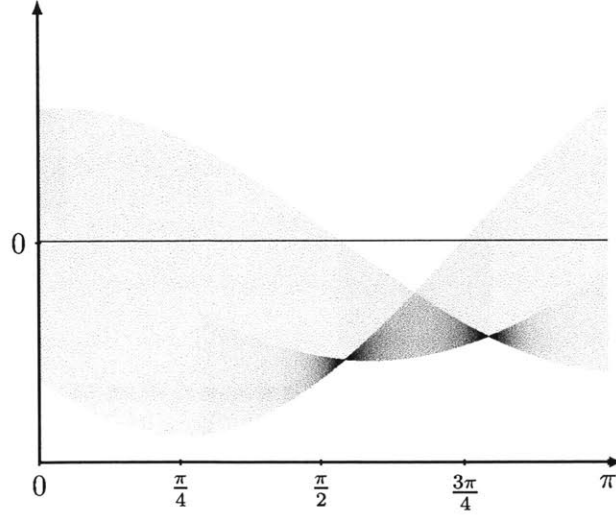


Figure 4-7: Intensity converted Radon transform sinogram of generic line segment L with $\alpha = 0.2$.

$$\mathbf{v}_{\Sigma 1} = (\mathbf{v}_2 + \mathbf{v}_1)/2 \quad \mathbf{v}_{\Sigma 2} = (\mathbf{v}_3 + \mathbf{v}_2)/2 \quad (4.32)$$

Then the Radon transform for our connected line segment object L_2 will be:

$$\mathcal{R}\mu_{L_2}(\boldsymbol{\theta}, s) = \frac{\alpha_1 \|\mathbf{v}_{\Delta 1}\|}{|\langle \mathbf{v}_{\Delta 1}, \boldsymbol{\theta} \rangle|} \text{rect} \left(\frac{s - \langle \mathbf{v}_{\Sigma 1}, \boldsymbol{\theta} \rangle}{\langle \mathbf{v}_{\Delta 1}, \boldsymbol{\theta} \rangle} \right) + \frac{\alpha_2 \|\mathbf{v}_{\Delta 2}\|}{|\langle \mathbf{v}_{\Delta 2}, \boldsymbol{\theta} \rangle|} \text{rect} \left(\frac{s - \langle \mathbf{v}_{\Sigma 2}, \boldsymbol{\theta} \rangle}{\langle \mathbf{v}_{\Delta 2}, \boldsymbol{\theta} \rangle} \right) \quad (4.33)$$

Figures 4-7 and 4-8 show plots of a sinogram and a circlegram respectively of measured intensity for a generic connected line segment object for $\alpha_1 = \alpha_2 = 0.2$, with black representing zero transmitted intensity and white begin unattenuated transmitted intensity I_0 .

We observe that just about every Radon projection looks like two adjacent rectangular functions, with the exception of three discrete projections. Two projection angles corresponding to the solutions to the two equations $\langle \mathbf{v}_{\Delta i}, \boldsymbol{\theta} \rangle = 0$ yield Radon transforms that look like a single rectangular function with delta function at one boundary of the rectangular function. A third projection angle also looks like a single rectangular function when the height of each adjacent rectangular function is the

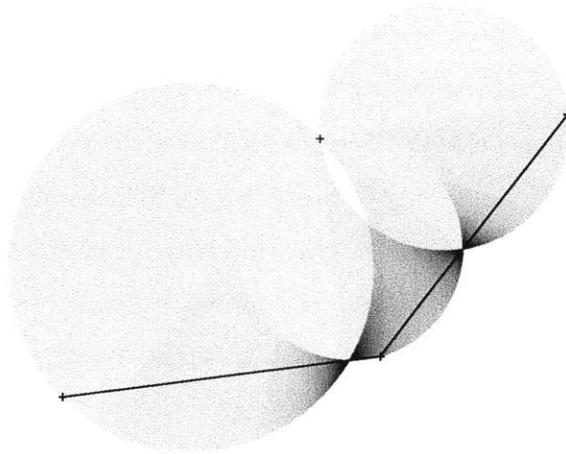


Figure 4-8: Intensity converted Radon transform circlegram of generic line segment L with $\alpha = 0.2$. A “+” marks the origin, with L drawn in black.

same: the projection angle θ for which the following equation is satisfied.

$$\frac{\alpha_1 \|\mathbf{v}_{\Delta 1}\|}{|\langle \mathbf{v}_{\Delta 1}, \boldsymbol{\theta} \rangle|} = \frac{\alpha_2 \|\mathbf{v}_{\Delta 2}\|}{|\langle \mathbf{v}_{\Delta 2}, \boldsymbol{\theta} \rangle|} \quad (4.34)$$

If the three vertices $(\mathbf{v}_1, \mathbf{v}_2, \mathbf{v}_3)$ are not collinear, there will only exist one solution to this equation. If the three vertices are collinear, the connected line segment will be identical to a single line segment discussed in the previous section.

4.3.1 Random Projections

When dealing with line segments, we have developed conditions for which Radon projections look normal, or behave as expected and do not degenerate into a special case. We have also seen that these degenerate cases occur at discrete projection angles. For the single line segment, there was one such projection angle: the projection angle which was perpendicular to the line segment itself. Now for connected line segments, there are three discrete projection angles that are degenerate, two projection angles that are perpendicular to the two line segments, and a third for which the measured intensities on either side of vertex \mathbf{v}_2 are equalized. In the case where $\alpha_1 = \alpha_2$, this projection angle corresponds to the direction of the bisector of the angle formed by

the two line segments. For a general connected chain of n vertices, there will be $(n - 1) + (n - 2) = 2n - 3$ degenerate projection angles.

In any case, these degenerate projection angles are discrete, and finite in number. Because these projection angles are discrete and finite in number, if we choose measurement projection angles randomly, we will choose a degenerate projection with probability zero. From now on, we will consider only random projection angles which will ensure that we will always obtain a generic measurement of the object.

4.3.2 Two Projections

Note that relating center and width measurements to edge lengths \mathbf{v}_Δ and edge centers \mathbf{v}_Σ is no longer trivial. For each Radon transform, there is a combinatorial ambiguity as to where each edge is located. For example, from each Radon projection are we observing two edges that are overlapping or adjacent? However, given random Radon projections, we are guaranteed to observe three discontinuities D_i corresponding to the projection of each vertex onto the projection angle:

$$D_i(\boldsymbol{\theta}) = \langle \mathbf{v}_i, \boldsymbol{\theta} \rangle \quad (4.35)$$

It is not known which discontinuity corresponds to which vertex, but because vertices \mathbf{v}_i must lie along backprojection lines, we can determine possible vertex locations based on backprojection line intersections for different projection angles. In addition to information about the locations of discontinuities, each Radon projection also provides information about the light attenuation through the two spaces bounded by each adjacent pair of discontinuities. This measured intensity will have three cases for the two line segment object:

$$I_i = I_0 \exp \left\{ \begin{array}{ll} -\frac{\alpha_1 \|\mathbf{v}_{\Delta 1}\|}{|\langle \mathbf{v}_{\Delta 1}, \boldsymbol{\theta} \rangle|} & \text{if edge 1 is present} \\ -\frac{\alpha_2 \|\mathbf{v}_{\Delta 2}\|}{|\langle \mathbf{v}_{\Delta 2}, \boldsymbol{\theta} \rangle|} & \text{if edge 2 is present} \\ -\frac{\alpha_1 \|\mathbf{v}_{\Delta 1}\|}{|\langle \mathbf{v}_{\Delta 1}, \boldsymbol{\theta} \rangle|} - \frac{\alpha_2 \|\mathbf{v}_{\Delta 2}\|}{|\langle \mathbf{v}_{\Delta 2}, \boldsymbol{\theta} \rangle|} & \text{if both edges are present} \end{array} \right\} \quad (4.36)$$

As with the single line segment object, it is impossible to resolve the ambiguity

inherent in identification with simply two projections and no prior knowledge of the attenuation coefficients for each edge. Figure 4-9 shows backprojections of two generic Radon projections for a sample two segment object L_2 . Instead of four possible vertex locations with two possible segments as was observed with the single line segment case, here we have nine possible vertex locations with 18 possible line paths. Table 4.1 shows a listing of the 18 possible line paths that could result in the given vertex backprojections.

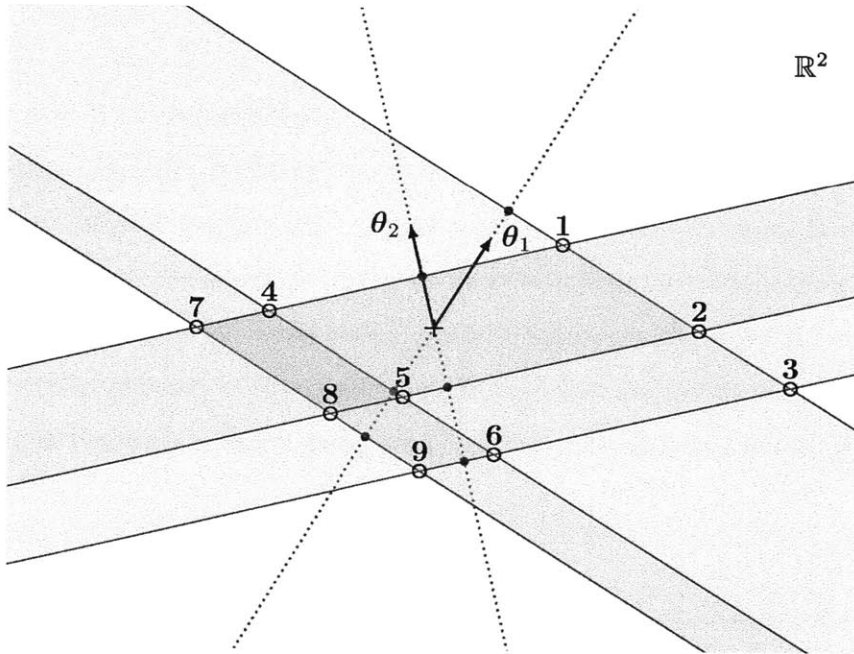


Figure 4-9: Backprojections for two generic Radon projections of a unknown connected line segment object L_2 . Possible vertex positions are circled and numbered.

However, we *can* further limit the possible paths by exploiting the measured intensities. Because we now have two line segments, it is possible that the two line segments might overlap for any given Radon projection. If they do overlap, the middle vertex v_2 will not be positioned in the middle position, and the measured intensity of the rectangular function adjacent to v_2 will be smaller and experience higher attenuation equal to the sum of the attenuations through each segment. More importantly, the measured intensity of the rectangular function adjacent to v will be smaller than the measured intensity of the other rectangular function.

| | | |
|-----|-----|-----|
| 159 | 249 | 348 |
| 195 | 267 | 357 |
| 168 | 276 | 375 |
| 186 | 294 | 384 |
| 618 | 429 | 438 |
| 519 | 627 | 537 |

Table 4.1: Vertex ordering of the 18 possible two segment paths given two generic Radon projections, without taking into account measured intensity. Each digit corresponds to the index of a vertex in Figure 4-9. The first digit corresponds to vertex v_1 of the segment, the second with vertex v_2 , and the third with vertex v_3 .

Therefore, having measured intensities of generic projections, we have knowledge of which rectangular function experiences higher attenuation (exhibits lower measured intensity) and, since v_2 can be adjacent only to the higher intensity rectangular function, we can limit the number of possible paths. In the example shown in Figure 4-9, vertices 1,2,3,6, and 9 correspond to impossible locations of the central vertex of the line path, thus we can further limit the possible paths to the eight paths in Table 4.1 having v_2 equal to indices 4,5,7, or 8. These possible paths are listed in Table 4.2.

| | | | |
|-----|-----|-----|-----|
| 159 | 357 | 249 | 348 |
| 276 | 375 | 186 | 384 |

Table 4.2: Vertex ordering of the eight possible two segment paths given two generic Radon projections, taking into account measured intensity. Each digit corresponds to the index of a vertex in Figure 4-9. The first digit corresponds to vertex v_1 of the segment, the second with vertex v_2 , and the third with vertex v_3 .

Without knowledge of the individual attenuation values α_i for each edge, we can gain no further information about our unknown object. However, if we know for example that both edges have the same attenuation value $\alpha_1 = \alpha_2$, then we can actually gain more information than had we only looked at each edge in isolation. Each of the eight possible paths that our connected line segment object might take have a known geometry. Given a single value of measured intensity, we can calculate the unique value of α that must exist for each possible path and store this listing of possible α values. These α values will be unique with probability 1 based on the

presumption of random projections. Identification of the correct value of α can be achieved by making a second such listing of possible α values for a different value of measured intensity and comparing the listings. Only one value of α will be common between the two listings, and this will be the correct value. Because this α value was associated with a specific path, this path must be the correct path, and the connected line segment object has been identified using only two projections.

4.4 Identification of Piecewise Linear Graphs

More general piecewise linear graphs of line segments can be evaluated in a similar manner to the two connected line segment case above. In the general case, the identification algorithm will require keeping track of all possible edge configurations of which there are an exponential number, $2^{(n-1)n/2}$. However, if we restrict ourselves to chains (only one or two connections per vertex), then the identification algorithm becomes computationally tractable, only having to keep track of a polynomial number of possible paths $O(n^5)$. Just as with two line segments, if α is known to be the same for all edges, then only two projections are needed for exact identification, while if α can be different for each segment, a third projection will be needed for exact identification.

4.5 Identification of Curved Surface Objects

Up until this point, we have only discussed the identification of piecewise linear surface objects defined by their vertices. In identifying piecewise linear surface objects, we compared the difference between adjacent values of measured intensity to essentially determine the amount of bending occurring at that point on the object. For connected strictly surface objects with constant attenuation coefficient along the path, we can adopt a similar algorithm. From three random Radon projections, the two endpoints of the curve can be identified from the discontinuities in the measured intensity of the Radon projection as we have discussed in identifying a single line object. The value of

the attenuation coefficient can be found from the discontinuity information as well in a similar manner as before. With a known value of the attenuation coefficient, a slope can be associated with every attenuating point on each Radon projection. In this way, the curve can be exactly reconstructed using the endpoints as boundary conditions after integrating the derivative of the curve found from the measured intensity. It is necessary to take into account the measured intensity from at least two non-orthogonal projections in order to resolve ambiguities that will arise from values of infinite slope.

Chapter 5

Conclusion

In this thesis we have defined an attenuation model for surface objects with negligible volume and algorithms for identifying these objects given a minimal set of random two dimensional Radon transform projections. Point objects require at least two projections to identify. Line segment objects require three Radon projections to identify, unless the attenuation coefficient is known, in which case two Radon projections are sufficient. Interestingly, connecting additional line segments with the same attenuation coefficient makes identification of the entire object's attenuation coefficient easier because of the ability to compare attenuation between segments. Piecewise linear chains consisting of two or more connected line segment objects with the same attenuation coefficient can be fully identified from only two projections. However, piecewise linear chains with variable attenuation coefficient still require three projections to identify. Lastly, general connected curved surfaces require three projections to identify based on their two endpoints and reconstruction of the object from the derivatives of its projections.

There is much future work to be done. This theory is easily extendable to three dimensional objects by analyzing two dimensional slices of the object. It is worth mentioning that interesting identification algorithms exist when directly analyzing three dimensional Radon projections of surface objects (vertices map to a sphere in three dimensional Radon space). However, it is of less practical interest as three dimensional Radon projections cannot be measured directly.

Also a question of considerable importance, but of substantial complexity is to analyze the proposed identification algorithms when spatial resolution and measurement accuracy are not perfect or with the addition of noise. This thesis was primarily concerned with providing a lower bound for the number of projections required to fully identify certain types of objects, and did not attempt to address this area of practical concern.

Appendix A

Notation

| | |
|--|--|
| x | scalar |
| θ | scalar angle |
| \mathbf{x} | vector |
| $\boldsymbol{\theta}$ | unit vector |
| $\ \mathbf{x}\ $ | Euclidean norm of vector \mathbf{x} |
| $\langle \mathbf{x}, \mathbf{y} \rangle$ | inner product of vectors \mathbf{x} and \mathbf{y} |
| \mathbb{R} | field of real numbers |
| \mathbb{R}^n | n-dimensional Euclidean space |
| S^{n-1} | unit n-sphere |
| $ A $ | Lebesgue measure of Euclidean subset A |
| $\{\mathbf{x} : P\}$ | Set of \mathbf{x} with property P |
| $X \mapsto Y$ | set X maps into set Y |
| $\mathcal{R}f$ | Radon transform of f |
| $\mathcal{F}f$ | Fourier transform of f |

Appendix B

MATLAB Code

B.1 Obtaining Projection Data

```
function [D,I] = projradon2(v,e,t,a)
% projradon2.m, 2D RADON PROJECTIONS
% Returns the discontinuity and intensity matrices for the 2D Radon transform
% given sparse 1D manifold data defined by vertices and edges
%
% Usage: [D,I] = r_proj2d(V,E,T,A)
%
% V - an nv x 2 matrix specifying the (x,y) coordinates of all nv vertices
%
% E - an ne x 3 matrix specifying the vertices and attenuation of all ne
% edges
%   Ei1 = index of first vertex v1 of edge
%   Ei2 = index of second vertex v2 of edge
%   Ei3 = normal attenuation of edge
%
% T - a vector of length nu specifying the nu sampled projection angles
%
% A - if E is ne x 2, program will pad E to ne x 3 with the constant value A
%
```

```

% D - an nv x nu matrix specifying the increasing sorted location of the ith
% discontinuity Dij at direction j
%
% I - an nv-1 x nu matrix specifying the measured intensity Aij between
% discontinuity Di and Di+1 at direction j
%
% Written by: Jason Ku, MIT
% Email: jasonku@mit.edu
% Created: July 2011

%% Input validation

nv = size(v,1);      % number of vertices
ne = size(e,1);      % number of edges
nu = numel(t);       % number of projection directions
D = zeros(nv,nu);    % sorted discontinuities per angle
I = zeros(nv-1,nu);  % sorted transmitted intensity per angle

if size(v,2) ~= 2
    disp('Error: V must have size(V,2) == 2');
    return
end
if size(e,2) ~= 3
    if size(e,2) == 2
        e = [e,ones(ne,1)*a];
    else
        disp('Error: E must have size(E,2) == 2|3');
        return
    end
end
if ~any(size(t) == 1)
    disp('Error: t must be a vector');

```

```

    return
end

%% Find D and I

u = [cos(t)',sin(t)'];           % convert t to unit vectors
u = u./diag(u*u').^0.5*ones(1,2); % normalize u
ue = v(e(:,1),:) - v(e(:,2),:); % ue - direction of edges
ue = ue./diag(ue*ue').^0.5*ones(1,2); % normalize ue
A = (e(:,3)*ones(1,nu))./abs(ue*u'); % A - attenuation wrt e and u
s = v*u';                       % s - projections wrt v and u
[D,ind] = sort(s,1,'descend');   % sort discontinuities
for i = 1:nu
    for j = 1:ne
        [ei,~] = find( ...       % fill I from vertex arrangement
            ind(:,i)*ones(1,2) == ...
            ones(nv,1)*[e(j,1),e(j,2)]);
        ei = sort(ei);           % loc of edge endpoints (ascend)
        for k = ei(1):ei(2)-1
            I(k,i) = I(k,i)+A(j,i); % add attenuation
        end
    end
end
end

end

end

```

B.2 Detecting Object Verticies

```

function [v] = detectradonvert2(D,I,t,lim)
% detectradonvert2.m, VERTEX DETECTION 2D
% Finds vertices from measured radon projections
%

```

```

% Usage: [V] = detectradonvert2(D,I,t)
%
% D - an nv x nu matrix specifying the increasing sorted location of the ith
% discontinuity Dij at direction j
%
% I - an nv-1 x nu matrix specifying the measured intensity Aij between
% discontinuity Di and Di+1 at direction j
%
% t - a vector of length nu specifying the nu sampled projection angles
%
% V - an nv x 2 matrix specifying the (x,y) coordinates of all nv vertices
%
% Written by: Jason Ku, MIT
% Email: jasonku@mit.edu
% Created: July 2011

%% Input validation

nv = size(D,1);      % number of vertices
nu = numel(t);      % number of projection directions

if size(D,2) ~= nu
    disp('Error: size(D,2) ~= numel(t)');
    return
end
if size(I,2) ~= nu
    disp('Error: size(I,2) ~= numel(t)');
    return
end
if size(D,1) ~= size(I,1)+1
    disp('Error: size(D,1) ~= size(I,1)+1');
    return

```

```

end
if ~any(size(t) == 1)
    disp('Error: t must be a vector');
    return
end
if nargin == 3; lim = 0; end

%% Detect Vertices

I = exp(-I);

% detect = [ones(1,nu); ...
%          (abs(I(2:nv-1,:)-I(1:nv-2,:))>lim); ...
%          ones(1,nu)];
%
% disp('Number of discontinuities observed')
% disp(['for each projection given lim = ',num2str(lim)])
% disp(sum(detect,1))

v = zeros(nv,2);
u = [cos(t)',sin(t)']; % convert t to unit vectors
u = u./(diag(u*u').^0.5*ones(1,2)); % normalize u
ve = zeros(nv,2);
l = 1;

for i = 1:nv
    for j = 1:nv
        ve(j,:) = [D(i,1)*u(1,:); ... % intersection of two backprojections
                  D(j,2)*u(2,:)] \ ... % D(i,1) and D(j,2)
                  [D(i,1)^2;D(j,2)^2];
    end
    for j = 1:nv

```

```

vf = [D(i,1)*u(1,:); ...      % intersection of two backprojections
      D(j,3)*u(3,:)]\ ...    % D(i,1) and D(j,3)
      [D(i,1)^2;D(j,3)^2];
for k = 1:nv                  % compare intersections to find match
    if all(abs(vf' - ve(k,:)) < 200*eps)
        v(1,:) = vf;
        l = l+1;
        break
    end
end
end
end
end
end
end

```

B.3 Detecting Object Edges

```

function [E] = detectradonedge2(D,I,t,V)
% detectradonedge2.m, EDGE DETECTION 2D
% Finds edges from measured radon projections
%
% Usage: [E] = detectradonvert2(D,I,t)
%
% D - an nv x nu matrix specifying the increasing sorted location of the ith
% discontinuity Dij at direction j
%
% I - an nv-1 x nu matrix specifying the measured intensity Aij between
% discontinuity Di and Di+1 at direction j
%
% t - a vector of length nu specifying the nu sampled projection angles
%
% V - an nv x 2 matrix specifying the (x,y) coordinates of all nv vertices

```



```

%
% Written by: Jason Ku, MIT
% Email: jasonku@mit.edu
% Created: July 2011

%% Input validation

nv = size(D,1);      % number of vertices
nu = numel(t);      % number of projection directions

if size(D,2) ~= nu
    disp('Error: size(D,2) ~= numel(t)');
    return
end
if size(I,2) ~= nu
    disp('Error: size(I,2) ~= numel(t)');
    return
end
if size(D,1) ~= size(I,1)+1
    disp('Error: size(D,1) ~= size(I,1)+1');
    return
end
if ~any(size(t) == 1)
    disp('Error: t must be a vector');
    return
end
%if nargin == 3; lim = 0; end

%% Detect Edges

%I = exp(-I);

```

```

% detect = [ones(1,nu); ...
%           (abs(I(2:nv-1,:)-I(1:nv-2,:))>lim); ...
%           ones(1,nu)];
%
% disp('Number of discontinuities observed')
% disp(['for each projection given lim = ',num2str(lim)])
% disp(sum(detect,1))

E = zeros(nv-1,3);
u = [cos(t(1)),sin(t(1))];
II = zeros(nv);

for i = 1:nv
    for j = 1:nv
        if j ~= i
            v = (V(i,:)-V(j,:))/norm(V(i,:)-V(j,:));
            II(i,j) = 1/abs(u*v');
        end
    end
end

measdiff = [I(1,1);I(2:end,1)-I(1:end-1,1);-I(nv-1,1)];

diff = zeros(nv,nv,nv);

for i = 1:nv
    for j = 2:nv
        for k = 1:j-1
            if i>j
                diff(j,k,i) = (-II(i,j)-II(i,k))/measdiff(i);
            else
                if i>k

```

```

        diff(j,k,i) = (II(i,j)-II(i,k))/measdiff(i);
    else
        diff(j,k,i) = (II(i,j)+II(i,k))/measdiff(i);
    end
end
end
end
end
end

a = 0;

[v1,v2] = find(diff(:,:,1));
for i = 1:numel(v1)
    if sum(sum(abs(diff(:,:,2)-diff(v1(i),v2(i),1))<5000*eps)) ~= 0
        a = diff(v1(i),v2(i),1);
    end
end

if a == 0
    disp('Alpha not found. ');
    return
end

%disp(['Alpha = ',num2str(1/a)]);
s = 1;
for i = 1:nv
    [j,k] = min(abs(diff(:,:,i)-a));
    [~,j] = min(j);
    k = k(j);
    %    disp('Edge detected between vertices: ');
    %    disp([num2str([i,j]),' and ',num2str([i,k])]);
end

```

```

    if i>j
        E(s,:) = [i,j,1/a];
        s=s+1;
    end
    if i>k
        E(s,:) = [i,k,1/a];
        s=s+1;
    end
end
end

E = E(1:s-1,:);

end

```

B.4 Plotting

```

function [] = plotsampradon2(D,I,t,type)
% plotradon2.m, PLOT RADON 2D
% Plots input radon transform in either (t,s) space or (x,y) space
%
% Usage: [] = plotradon2(D,I,t,type)
%
% D - an nv x nu matrix specifying the increasing sorted location of the ith
% discontinuity Dij at direction j
%
% I - an nv-1 x nu matrix specifying the measured intensity Aij between
% discontinuity Di and Di+1 at direction j
%
% t - a vector of length nu specifying the nu sampled projection angles
%
% type - 'rect' or 'polar' plot preference, 'rect' default
%

```

```

% Written by: Jason Ku, MIT
% Email: jasonku@mit.edu
% Created: July 2011

%% Input validation

nv = size(D,1);          % number of vertices
nu = numel(t);          % number of projection directions
I = exp(-I);

if size(D,2) ~= nu
    disp('Error: size(D,2) ~= numel(t)');
    return
end
if size(I,2) ~= nu
    disp('Error: size(I,2) ~= numel(t)');
    return
end
if size(D,1) ~= size(I,1)+1
    disp('Error: size(D,1) ~= size(I,1)+1');
    return
end
if ~any(size(t) == 1)
    disp('Error: t must be a vector');
    return
end
if nargin == 4 && strcmp(type,'rect') && strcmp(type,'polar')
    disp('Error: type must be rect or polar');
    return
end

%% Prepare figure

```

```

clf(gcf);
set(gcf,'Color','w');
hold on
axis off

%% Plot rect

if nargin == 3 || strcmp(type,'rect')

    for i = 1:nu-1
        for j = 1:nu-1
            patch([t(j),t(j),t(j+1),t(j+1)]*180/pi, ...
                [D(i,j),D(i+1,j),D(i+1,j),D(i,j)], ...
                'k','FaceColor',[1,1,1]*(I(i,j)), ...
                'EdgeColor','none');
        end
        patch([t(nu),t(nu),t(1)+pi,t(1)+pi]*180/pi, ...
            [D(i,nu),D(i+1,nu),D(i+1,nu),D(i,nu)], ...
            'k','FaceColor',[1,1,1]*(I(i,nu)), ...
            'EdgeColor','none');
    end
    plot([0,179],[0,0],'k')
    xlim([-1,180]);
end

%% Plot polar

if strcmp(type,'polar')
    u = [cos(t)',sin(t)'];
    temp = u(nu,:);
    ang = zeros(nu,1);

```

```

for i = nu:-1:2
    ang(i) = acos(u(i,:)*u(i-1,:))/2;
    u(i,:) = (u(i-1,:)+u(i,:))/norm(u(i-1,:)+u(i,:))/cos(ang(i));
end
ang(1) = acos(-u(1,:)*temp)/2;
u(1,:) = (u(1,:)-temp)/norm(u(1,:)-temp)/cos(ang(1));
for i = 1:nv-1
    for j = 1:nu-1
        p = [u(j,:)*D(i,j);u(j,:)*D(i+1,j); ...
            u(j+1,:)*D(i+1,j);u(j+1,:)*D(i,j)];
        patch(p(:,1),p(:,2), ...
            'k','FaceColor',[1,1,1]*(I(i,j)), ...
            'EdgeColor','none');
    end
    p = [u(nu,:)*D(i,nu);u(nu,:)*D(i+1,nu); ...
        -u(1,:)*D(i+1,nu);-u(1,:)*D(i,nu)];
    patch(p(:,1),p(:,2), ...
        'k','FaceColor',[1,1,1]*(I(i,nu)), ...
        'EdgeColor','none');
end
plot(0,0,'k+')
axis equal
end

end

```


Bibliography

- [1] Udo Jochen Birk, Alex Darrell, Nikos Konstantinides, Ana Sarasa-Renedo, and Jorge Ripoll. Improved reconstructions and generalized filtered back projection for optical projection tomography. *Appl. Opt.*, 50(4):392–398, Feb 2011.
- [2] Nicholas D. Blakeley, P. J. Bones, R. P. Millane, and Peter Renaud. Efficient frequency-domain sample selection for recovering limited-support images. *J. Opt. Soc. Am. A*, 20(1):67–77, Jan 2003.
- [3] David J Brenner and Eric J Hall. Computed tomography an increasing source of radiation exposure. *Most*, 357(22):2277–2284, 2007.
- [4] Andrei V. Bronnikov and Gerrit Duifhuis. Wavelet-based image enhancement in x-ray imaging and tomography. *Appl. Opt.*, 37(20):4437–4448, Jul 1998.
- [5] Anne Dominique Cambou and Narayanan Menon. Three-dimensional structure of a sheet crumpled into a ball. *Proceedings of the National Academy of Sciences*, 2011.
- [6] E. J. Candes, J. Romberg, and T. Tao. Robust uncertainty principles: exact signal reconstruction from highly incomplete frequency information. *IEEE Transactions on Information Theory*, 52(2):489–509, February 2006.
- [7] E. J. Candes and M. B. Wakin. An introduction to compressive sampling. *IEEE Signal Processing Magazine*, 25(2):21–30, March 2008.
- [8] R. Clack and M. Defrise. Cone-beam reconstruction by the use of radon transform intermediate functions. *J. Opt. Soc. Am. A*, 11(2):580–585, Feb 1994.
- [9] J.P. Earls and J. Leipsic. Cardiac computed tomography technology and dose-reduction strategies. *Radiol Clin North Am*, 48(4):657–74, 2010.
- [10] Daissy H. Garces, William T. Rhodes, and Nestor M. Peña. Projection-slice theorem: a compact notation. *J. Opt. Soc. Am. A*, 28(5):766–769, May 2011.
- [11] G. Harding. X-ray scatter tomography for explosives detection. *Radiation Physics and Chemistry*, 71(3-4):869 – 881, 2004. 9th International Symposium on Radiation Physics (ISRP-9).
- [12] E. Hecht. *Optics*. Addison-Wesley, 2002.
- [13] H.J. In, S. Kumar, Y. Shao-Horn, and G. Barbastathis. Nanostructured origami trade; 3d fabrication and assembly of electrochemical energy storage devices. In *Nanotechnology, 2005. 5th IEEE Conference on*, pages 374 – 377 vol. 1, July 2005.

- [14] M. Lesaffre, S. Farahi, A. C. Boccara, F. Ramaz, and M. Gross. Theoretical study of acousto-optical coherence tomography using random phase jumps on ultrasound and light. *J. Opt. Soc. Am. A*, 28(7):1436–1444, Jul 2011.
- [15] Michael Lustig, David Donoho, and John M. Pauly. Sparse mri: The application of compressed sensing for rapid mr imaging. *Magnetic Resonance in Medicine*, 58(6):1182–1195, 2007.
- [16] A. Markoe. *Analytic tomography*. Encyclopedia of mathematics and its applications. Cambridge University Press, 2006.
- [17] F. Natterer. *The mathematics of computerized tomography*. Classics in applied mathematics. Society for Industrial and Applied Mathematics, 2001.
- [18] D. Tack and P.A. Gevenois. *Radiation dose from adult and pediatric multidetector computed tomography*. Medical Radiology. Springer, 2007.
- [19] Heang K. Tuy. An inversion formula for Cone-Beam reconstruction. *SIAM Journal on Applied Mathematics*, 43(3):546–552, 1983.